Geostrophic equatorial deep jets

by Charles C. Eriksen[1]

ABSTRACT

Deep zonal jets in the western Pacific are geostrophic in character at latitudes of a fraction of a degree. This evidence corroborates the interpretation that deep jets very close to the equator take the form of Kelvin waves. Vertical displacements inferred from GEOSECS density profiles in the Pacific and Atlantic suggest deep jets are a general feature of equatorial oceans.

1. Introduction

Deep current jets confined to the equator have been observed from just beneath the thermocline to nearly the ocean floor in both the Pacific and Indian Oceans using acoustic dropsonde techniques (Luyten and Swallow, 1976; Eriksen, 1981; Hayes and Milburn, 1980). Deep current profiles have yet to be measured in the equatorial Atlantic, but, as will be demonstrated herein, density profiles suggest that deep jets are a general feature of the equatorial oceans. These deep jets have been documented because of the development of acoustic dropsondes, where currents are inferred from the trajectory of a freely falling probe. Not surprisingly, deep jets have an associated vertical displacement (potential energy) signal which is manifested as perturbations of density profiles. The density signal is small (typical perturbations correspond to temperature changes of a few hundredths of a degree C) but is also of small vertical scale (vertical wave lengths of a few hundred meters) which is why it can be detected from a Conductivity-Temperature-Depth (CTD) profiler survey over the appropriate horizontal scales.

This work is an extension of work we did in the western Pacific (Eriksen, 1981) using an acoustic dropsonde called the Whitehorse, which included a CTD (see Luyten *et al.*, 1982 for a description of the instrument and its performance). We concluded from that study that within about 100 km of the equator, deep jets had the characteristics of Kelvin waves. This conclusion was drawn, among other considerations, from the relationship between density and zonal currents found in the observations. We will strengthen this conclusion by demonstrating the geostrophic nature of deep jets very close to the equator. Evidence from deep CTD profile

1. Department of Earth and Planetary Sciences and Department of Meteorology and Physical Oceanography, Massachusetts Institute of Technology, Cambridge, Massachusetts, 02139, U.S.A.

surveys at the same and other locations suggests that similar current-density features exist in other parts of the Pacific and in the Atlantic as well. The geostrophic comparisons are from Whitehorse profiles. The other density profiles were collected from 1972 to 1974 in the Geochemical Ocean Sections Study (GEOSECS) and made available in edited calibrated form in 1980.

Section 2 is a discussion of properties of equatorial waves detectable in profiles, including the relationship between zonal current and displacements. Section 3 contains comparisons of geostrophic with Whitehorse profiles, and Section 4 is a discussion of why geostrophic currents can be detected at very low latitudes. Section 5 reviews the method of calculating vertical displacements and Section 6 discusses the results of GEOSECS data. A discussion with conclusions appears in Section 7.

2. Detection of equatorial waves with profile data

Profiles taken from a ship are suitable for detecting low frequency equatorial waves, since a survey pattern can be completed faster than substantial temporal changes of the waves can occur. Since frequency spectra tend to be red, the low frequency structures dominate higher frequency phenomena in energy. A characteristic of equatorial waves is that their deformation radius is determined by vertical scale, stratification, and β, the change of Coriolis parameter with latitude. A collection of profiles from a single ship survey constitutes a snapshot (the result of a broad band of frequencies) which can be analyzed for its horizontal structure as a function of vertical scale. The vertical wavenumber auto-spectra of different flow variables and their cross-spectra provide clues to the mixture of wave types present. Eriksen (1981) used this approach to interpret current and density profiles from the western Pacific. A brief reminder of the properties of equatorial waves is appropriate here, including an explanation of a key characteristic of equatorial profiles: the relative phase of zonal velocity and vertical displacement.

The solutions to the Boussinesq, inviscid, linearized equations of motion on an equatorial beta plane ($f = \beta y$) take the form

$$\begin{vmatrix} u \\ v \\ p \\ \zeta \end{vmatrix} = \sum_{n,m} A_{nm}\, e^{i(kx-\omega t)} \begin{vmatrix} U_n(y/y^*_m)\, G'_m(z) & \text{(1a)} \\ i\, V_n(y/y^*_m)\, G'_m(z) & \text{(1b)} \\ C_m\, P_n(y/y^*_m)\, G'_m(z) & \text{(1c)} \\ C_m^{-1}\, P_n(y/y^*_m)\, G_m(z) & \text{(1d)} \end{vmatrix}$$

where u,v,p, and ζ are eastward current, northward current, pressure, and vertical displacement, respectively. A wave component with vertical variation $G_m(z)$ has a characteristic horizontal phase velocity $C_m = \sqrt{gh_m}$ (where h_m is an equivalent depth) and a characteristic meridional scale $y^*_m = (C_m/\beta)^{\frac{1}{2}}$. There are four classes of meridional wave functions: Kelvin, mixed Rossby-gravity, Rossby, and gravity

waves. If n is odd (even) V_n has odd (even) symmetry about the equator and vice versa for both U_n and P_n. For more on the properties of these waves, see Moore and Philander (1977), Wunsch and Gill (1976) and Eriksen (1980).

The coherence phase of u with ζ is determined by the sign of $U_n \cdot P_n$ for the waves which dominate the spectrum at a particular latitude. For Kelvin and mixed Rossby-gravity waves, this product is positive indefinite for all latitudes. As shown in Appendix A, Rossby and gravity waves with eastward phase velocity also have $U_n \cdot P_n > 0$ near the equator so that vertical displacement leads eastward current with increasing depth (decreasing z) by $\pi/2$ since $u \propto G'(z)$ and $\zeta \propto G(z)$. For Rossby and gravity waves of westward phase velocity, $U_n \cdot P_n < 0$ so vertical displacement lags eastward current with depth. The phase relationship between u and ζ in depth is the same for both vertically standing and propagating waves. These statements hold true for latitudes equatorward of the first zero crossing of either U_n or P_n. For even n, $U_n = P_n = 0$ at $y = 0$ but $U_n \cdot P_n$ has the same sign for absolute latitudes $| y | \neq 0$. Thus, if observed coherence of u and ζ at $y = 0$ is significant and the two variables are in quadrature, the sign of the phase can be interpreted as indicative of the direction of zonal phase propagation of the waves which dominate the cross-spectra. Mixed Rossby-gravity waves with westward phase speeds are the only exception to the rule that near the equator $U_n \cdot P_n$ has the same sign as the zonal wavenumber of the waves.

If only density profiles are available (no direct measurements of current, as well), geostrophic approximations to zonal current can be computed from meridional sections. At low frequencies, the zonal component of current is nearly geostrophic for long Rossby modes (in the nondispersive limit) and exactly geostrophic for Kelvin modes. Short Rossby and mixed Rossby-gravity modes at low frequency have negligible zonal current at all latitudes. Thus low frequency equatorial waves which produce strong zonal currents are likely to be either of the nondispersive Rossby or the Kelvin type. For Rossby waves, potential energy is much less than kinetic energy near the equator (see Appendix B), but for Kelvin waves energy is in equipartition everywhere between potential and zonal kinetic. This means that density profiles which show maximum amplitude in vertical displacement near the equator suggest Kelvin waves. Geostrophically computed eastward velocity will, of necessity, lag vertical displacement by $\pi/2$ in depth in this case. This phase relation is reversed for profiles in which vertical displacement amplitudes grow from the equator (as in nondispersive Rossby waves). If both Kelvin and Rossby waves are present, the Kelvin waves will dominate the geostrophically computed zonal currents near the equator.

These remarks apply to the observations of deep equatorial jets in the western Pacific (Eriksen, 1981) made with the Whitehorse. The jets were primarily zonal in character, coherent and in phase from 3/4S to 3/4N, and of amplitudes 5-20 cm/s at vertical scales of hundreds of meters. The variation due to changes in buoyancy

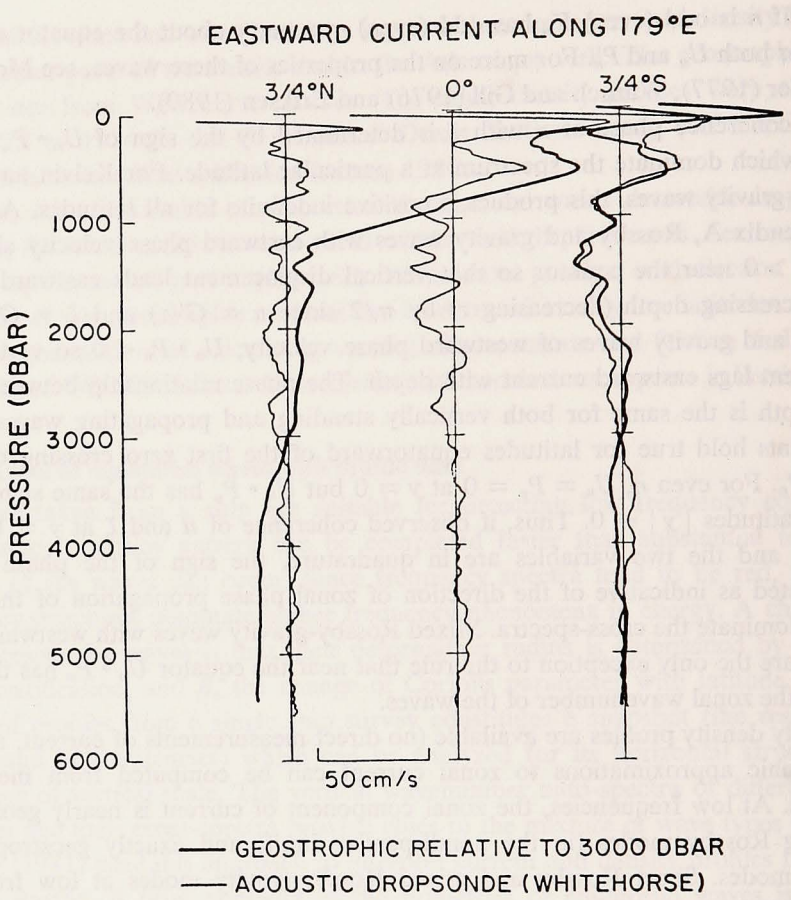

Figure 1. Profiles of geostrophic eastward current relative to 3000 dbar (heavy traces) at 3/4N and 3/4S superimposed on the directly measured current traces along 179E made on 27 and 28 May, 1978. Note the visual similarity of the geostrophic and directly measured current traces over vertical wavelengths of a few hundred meters: the deep jets.

frequency $N(z)$ were removed by WKBJ stretching so that standard spectral analysis techniques could be applied. Near the equator, vertical displacement inferred from the density profiles did, indeed, lead zonal current by $\pi/2$ with depth, suggesting these jets are Kelvin waves very close to the equator. The geostrophic nature of the jets is discussed next.

3. Geostrophic and directly measured zonal velocity comparisons

Traditional geostrophic computations were made for the CTD profiles taken in the western Pacific with one modification: meridional dynamic height at each pressure was fit using piecewise cubic splines instead of first differences. This fit was done to make the meridional derivative of dynamic height vary smoothly at the

latitudes of stations. The Whitehorse profiles reported in Eriksen (1981) were made along 179E (two sections roughly six days apart) and 168E (one section). At the vertical scales resolvable in the profiles, it is only at the stations nearest the equator (3/4N, 3/4S) that we expect to be able to estimate current geostrophically and have it compare favorably with dropsonde measurements. More on the expected success of geostrophic calculations near the equator on short vertical scales is presented in the next section.

In all six comparisons between directly measured and geostrophic currents the short scale features are visually similar. An example of a comparison is shown in Figure 1. Note the strong resemblance of geostrophic to Whitehorse directly measured current at 3/4S. At 3/4N there is a noticeable shear of large vertical scale superimposed upon smaller scale features whose extrema are similar to those in the dropsonde profile of the same scale. Clearly, geostrophic currents at large vertical scale 0(1000 m) or more bear little resemblance to directly measured currents. However, the deep jets are described remarkably faithfully by geostrophy. The reader should keep in mind that the Whitehorse density and current profiles are collected virtually independently.

A quantitative comparison of Whitehorse zonal current and geostrophic current at 3/4° latitude is given in Figures 2a and 2b. Six profiles (3/4N and 3/4S; two each at 179E, one each at 168E, see Table 2 for details of the station data) are piece averaged and five adacent wavenumber estimates are averaged to form these autospectra and coherences. These spectral estimates are formed from WKBJ stretched series (identical to the treatment in Eriksen, 1981); due to nonuniform vertical resolution in the stretched vertical coordinate, wavenumber estimates higher than about 0.005 cycles per stretched decibar ("cpsd") are suspect. Estimates at the very lowest wavenumber plotted in each figure are also unreliable, since these have half the statistical reliability and may also suffer the effects of incomplete removal of trends in the data. The four estimates at stretched wavelengths at 800, 400, 268, and 200 dbar are the only ones which should be considered seriously. In this range the geostrophic estimate goes from overestimating zonal kinetic energy by a factor of two to underestimating it by a factor of ten (Fig. 2a). Obviously geostrophic estimates of zonal energy density are unreliable; what is remarkable is that they are as good as they are. The accuracy of this method depends on vertical wavenumber as a function of latitude (as will be discussed in the next section). Figure 2b shows that the Whitehorse and geostrophic currents are coherent at zero phase at 95% confidence at the wavelengths mentioned above. This is expected from the visual similarities of the traces (e.g., Fig. 1).

4. Equatorial limitations of geostrophic estimation

It is clear from the comparisons discussed above that geostrophic estimation of

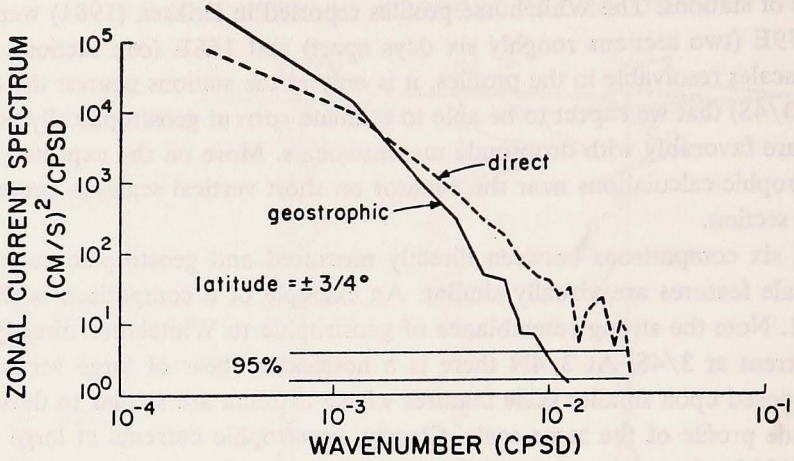

Figure 2. (a) Autospectra of, and (b) coherence between zonal currents measured directly and geostrophically from 6 Whitehorse profiles. Wavenumber averaging over 5 adjacent bands leads to error bars and level of no significance based on Koopmans (1974). "CPSD" means cycles per stretched decibar, where stretching is relative to an ocean with $N = 1$ cph.

short vertical scale features is moderately successful at latitudes so low that error sources in density profiles render large vertical scale estimates useless. The conventional method for calculating currents geostrophically is to compute dynamic height ΔD (λ,ϕ,p) relative to some reference pressure surface p_o for each density cast taken at latitude ϕ, longitude λ and approximate the horizontal gradient of ΔD numerically. Near the equator the Coriolis parameter $f = 2\Omega \sin \phi$ becomes very small so that small dynamic height differences between stations imply rather large geostrophic currents. Errors of at least two types accrue in estimates of ΔD (an integral of specific volume anomaly in pressure): those due to a calibration offset in density (e.g., a salinity offset ΔS) and those due to random noise in the individual density estimates at each pressure.

Errors of the offset type lead to inferred uniform shears between stations as can be seen from examination of the geostrophic approximation:

$$U(p) - U(p_o) = -(fr)^{-1} \frac{\partial}{\partial \phi} \int_{p_o}^{p} \delta dp = -(fr)^{-1} \frac{\partial}{\partial \phi} \Delta D \qquad (2)$$

where δ is specific volume anomaly (*in situ* specific volume minus specific volume at salinity 35 p.s.u. and temperature 0°C) and r is the radius of the earth. As an example, a salinity offset of only 0.001 p.s.u. between stations will lead to a geostrophic shear of about 10 cm/s/km at 0°30′ latitude. Absolute calibration of CTD profiles can be done to about ± 0.003 p.s.u., ± 0.015°C temperature, and ± 1.5

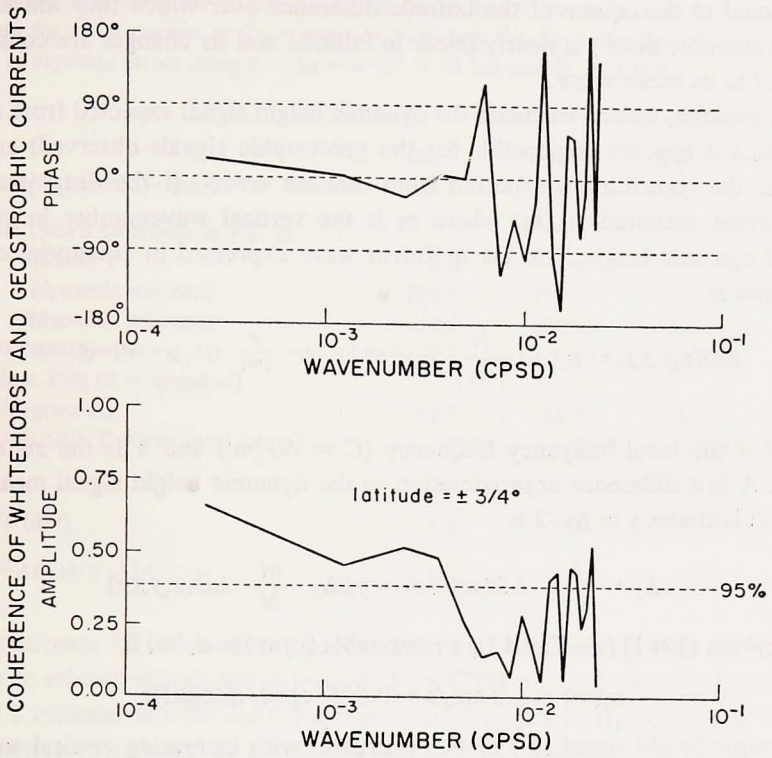

dbar pressure (Fofonoff *et al.*, 1974). However, in computing dynamic height it is the calibration *difference* between neighboring stations that is important. In the Whitehorse stations, for example, deep potential temperature-salanity traces were adjusted to be the same to within ± 0.001 p.s.u. in salinity over the range $1.3 < \theta < 1.5$°C and to be within the $\theta - S$ scatter of deep bottle stations. Even so, 10 cm/s/km is an intolerably large error in geostrophic shear if scales of 0(1 km) depth are of interest. The deep jets, however, have much smaller vertical scales (0(100 m)) so they can be extracted despite calibration error.

Random errors in density, to the extent that they can be considered independent, are less serious than systematic ones such as those discussed above. Suppose random salinity errors are ± 0.001 p.s.u. for each 2 dbar average in CTD profiles. The "random walk" in dynamic height will be proportional to the square root of the number of independent estimates so that over 200 dbar, geostrophic shear due to this error will be only about 1 cm/s/km at 0°30′ latitude. The salinity scatter in deep $\theta - S$ traces in the Whitehorse profiles is of this size or smaller. The error in shear is proportional to the inverse square root of the depth difference over which it is estimated, instead of being independent of depth difference as errors due to systematic errors in density are. Zonal shear errors of both kinds are inversely

proportional to the square of the latitude difference over which they are estimated near the equator, since f is nearly linear in latitude and its changes are considerable compared to its mean value.

As an exercise, we can calculate the dynamic height signal expected from a Kelvin wave (since it appears responsible for the geostrophic signals observed) and compare it to the contribution expected from random errors. If the deep jets have a zonal current amplitude $u_o(m)$ where m is the vertical wavenumber in cpsd, the expected dynamic height field for a Kelvin wave expressed in equatorial cartesian coordinates is

$$\Delta D(x,y,z,t) = u_o(m)\frac{N}{|m|}\, e^{i(\pm mz + k\,(x - \frac{N}{|m|}t))}\; e^{-(y^2|m|\beta/2N)} \tag{3}$$

where N is the local buoyancy frequency ($C = N/|m|$) and k is the zonal wavenumber. A first difference approximation to the dynamic height signal measured at stations at latitudes $y \pm \Delta y/2$ is

$$\Delta y \cdot \frac{\partial}{\partial y}\; \Delta D(x,y,z,t) = y\beta\Delta y\; \frac{m}{N}\; \Delta D(x,y,z,t) \tag{4}$$

From Eriksen (1981) (his Fig. 13), a reasonable form for $u_o(m)$ is

$$u_o(m) = 1.0\ \text{cm/s} \cdot (0.005\ \ \text{cpsd/m(cpsd)}) \tag{5}$$

The dynamic height signal ((3) or (4)) decreases with increasing vertical wavenumber faster than the contribution from random error. The contribution from random error can be written as

$$\Delta(\Delta D) \approx (2\pi/m\Delta p)^{1/2} \cdot \delta S \cdot \Delta p \cdot \frac{\partial \alpha}{\partial S} \tag{6}$$

where $2\pi/m$ is the scale of the Kelvin wave and $\delta S \cdot \partial\alpha/\partial S$ is the specific volume error arising from random salinity errors in each CTD estimate at pressure interval Δp. The number of independent estimates is then $2\pi/m\Delta p$, so the total error in the random walk goes as the square root of this number. Using $y = \Delta y = 3/4°$, $\delta S = 0.001$ p.s.u., $\Delta p = 2$ dbar, and $\partial\alpha/\partial S = 7 \times 10^{-4}$ cm^3/g/p.s.u. and $u_o(m)$ specified by (5) leads to the model estimates in Table 1. For reference, the equatorial radius of deformation is listed for $N = 1.0$ cph. Following that, the dynamic height amplitude at the equator, dynamic height amplitude at 3/4° latitude, specific volume anomaly amplitude at the equator, and approximate equivalent temperature or salinity amplitudes in an isohaline or isothermal ocean are listed. The ratios of dynamic height signal to random noise of a comparable scale are a guide to how successful geostrophic detection of Kelvin waves might be. A ratio larger than unity is desirable. The meridional station spacing influences which wavenumber band will be measured best. Although the amplitudes are in the range of 0(10-100)

Table 1. Some representative Kelvin wave amplitudes based on a given vertical wavenumber spectrum for zonal current at the equator ($y = 0$) (see Eq. 5), and ratios of dynamic height signals to expected errors using $y = \Delta y = 0°45' = 83$ km and $N_* = 1$ cph.

	Vertical wavelength (stretched dbar)			
	800	400	268	200
Radius of deformation y_* (km)	99	70	57	49
Amplitudes (based on model in Eq. 5)				
$u(0)$ (cm/s)	4.0	2.0	1.3	1.0
$\Delta D(0)$ (dynamic microns)	888.9	222.2	98.8	55.6
$\Delta D(y)$ (dynamic microns)	622.5	109.0	33.9	13.4
$\delta(0)$ (10^{-4}cm^2/g)	27.8	7.0	3.1	1.7
Equivalent $T(0)$ (S = constant) (millidegrees C)	231.7	58.0	25.8	14.5
Equivalent $S(0)$ (T = constant) (p.s.u.)	.0379	.0095	.0042	.0024
Ratios				
$\Delta D(y)/\Delta(\Delta D)$	8.87	2.20	0.84	0.38
$\Delta y \frac{\partial}{\partial y} \Delta D(y)/\Delta(\Delta D)$	6.32	3.13	1.79	1.09

dynamic microns ($0(10^{-4}-10^{-3})$ joules/kg), the equivalent specific volume, temperature or salinity signals are detectable by a CTD relatively easily. The numbers in Table 1 indicate that the density signature of deep jets of the amplitude observed (e.g., equation (5)) should be detectable with a CTD, but not with Nansen bottles, for example.

5. Method of calculating vertical displacements

A convenient way of estimating potential energy fluctuations for time dependent motions is to calculate vertical displacement of isopycnals from their mean position. For low frequency motions, determining the temporal mean is generally unfeasible. Instead, a mean potential density profile and its derivative can be calculated by averaging stations along a meridian, for example. It is assumed that zonal changes have larger horizontal scale than meridional ones (this is true for low frequency equatorial waves) so that a transect not strictly along a meridian can be used. It is also assumed that meridional variability is sufficiently rich and sufficiently well sampled by close station spacing that a spatial average represents a temporal average (an assumption of ergodicity is implied). Structures whose scale is much greater than the averaging domain (say 2-4° either side of the equator) will not be detected by this method. Finally it is assumed that deviations in individual profiles from the mean are due to vertical advection only. The most convincing evidence that this method gives realistic vertical displacement estimates is that they are coherent with current profiles measured by independent means. Moreover, displace-

ments inferred using an average profile from Whitehorse plus GEOSECS stations to form a mean profile are indistinguishable from those formed from Whitehorse stations only.

To compare results from different oceans and different CTD instruments, it is important to use a uniform data reduction procedure. The basic calibrated edited data are pressure series of temperature and salinity formed from averages over 2 dbar for the Whitehorse and 2.5 dbar for GEOSECS. Displacements were calculated according to the algorithm described by Eriksen (1981) on a 20 dbar grid. Average profiles were made for the general geographic region of the transects.

GEOSECS transects cross the equator twice in the Atlantic and Pacific Oceans, thrice in the Indian Ocean (see Broecker (1981) for a description of the experiment and discussion of bottle data). Unfortunately, only the transects at 179E and 124W in the Pacific, and 36W in the Atlantic have sufficiently dense station spacing ($\lesssim 2°$) near the equator to make them useful for detecting equatorial jets from density profiles. The stations used are listed in Table 2.

To form estimates of potential energy wavenumber spectra that can be compared at different locations, the displacements are assumed to scale in a WKBJ manner (i.e., vertical displacement is proportional to $(N_o/N(z))^{\frac{1}{2}}$ where $N_o = 1$ cph is an arbitrary reference buoyancy frequency and $N(z)$ is the local value, and vertical scales are proportional to $N(z)/N_o$). The potential energy spectral density can be estimated as $\frac{1}{2} N_o^2$ times the spectrum of stretched vertical displacement.

6. GEOSECS vertical displacement spectra

Vertical displacement spectra in the western Pacific are not as strongly enhanced at the equator as zonal current spectra (Eriksen, 1981), in fact, in the band centered at 800 stretched dbar they are less energetic at the equator than at latitudes of a few degrees. The GEOSECS data along 179E are similarly enhanced at the equator for all but the 0.00125 cpsd band (Fig. 3) and appear to be enhanced near the equator for all wavenumber bands considered at 124W and 36W. Spectra are computed by both piece (station) and wavenumber band averaging in the same manner as for currents discussed above. Although the error bars drawn do not always indicate statistically distinguishable enhancement for profiles at the equator in a given vertical wavenumber band, the general latitudinal shape of spectra is similar for different bands so that further band averaging increases statistical reliability to the point that spectral estimates are distinguishable at the 95% confidence level.

In the GEOSECS displacements, just as in the Whitehorse displacement (plotted for reference), the vertical displacement energy increases equatorward of 1° latitude for all but the 800 stretched dbar wavelength. We compare vertical displacements instead of geostrophic currents because they do not depend on the meridional differencing scheme employed.

Table 2. CTD stations used to form vertical displacement profiles.

Mean profile group	Date	Latitude	Longitude
Along 179E			
Whitehorse	25 May 1978	3°00′N	179°00′E
	26 May 1978	1°30′N	179°00′E
	27 May 1978	0°45′N	179°00′E
	28 May 1978	0°00′	179°00′E
	28 May 1978	0°45′S	179°00′E
	29 May 1978	1°30′S	179°00′E
	30 May 1978	3°00′S	179°00′E
	31 May 1978	0°00′	179°00′E
	1 Jun 1978	3°00′N	179°00′E
	1 Jun 1978	1°30′N	179°00′E
	2 Jun 1978	0°45′N	179°00′E
	3 Jun 1978	0°00′	179°00′E
	3 Jun 1978	0°45′S	179°00′E
	4 Jun 1978	1°30′S	179°00′E
GEOSECS			
	19 Dec 1973	3°04′N	178°55′E
	19 Dec 1973	2°00′N	178°56′E
	20 Dec 1973	1°01′N	178°55′E
	21 Dec 1973	0°31′N	178°59′E
	21 Dec 1973	0°00′	179°00′E
	22 Dec 1973	0°28′S	178°59′E
	22 Dec 1973	1°02′S	179°02′E
	23 Dec 1973	2°01′S	179°01′E
	23 Dec 1973	2°59′S	178°59′E
Along 168E			
Whitehorse	8 Jun 1978	1°30′S	168°00′E
	9 Jun 1978	0°45′S	168°00′E
	9 Jun 1978	0°00′	168°00′E
	10 Jun 1978	0°45′N	168°00′E
	10 Jun 1978	1°30′N	168°00′E
	11 Jun 1978	3°00′N	168°00′E
Along 124W			
GEOSECS	26 May 1974	1°30′S	124°40′W
	27 May 1974	0°04′N	124°34′W
	27 May 1974	1°32′N	124°32′W
	28 May 1974	3°01′N	124°22′W
Along 36W			
GEOSECS	21 Oct 1972	2°00′N	37°21′W
	21 Oct 1972	0°58′N	37°04′W
	22 Oct 1972	0°31′N	36°31′W
	22 Oct 1972	0°01′N	35°58′W
	23 Oct 1972	0°30′S	34°59′W
	23 Oct 1972	0°59′S	34°02′W
	24 Oct 1972	1°58′S	32°31′W

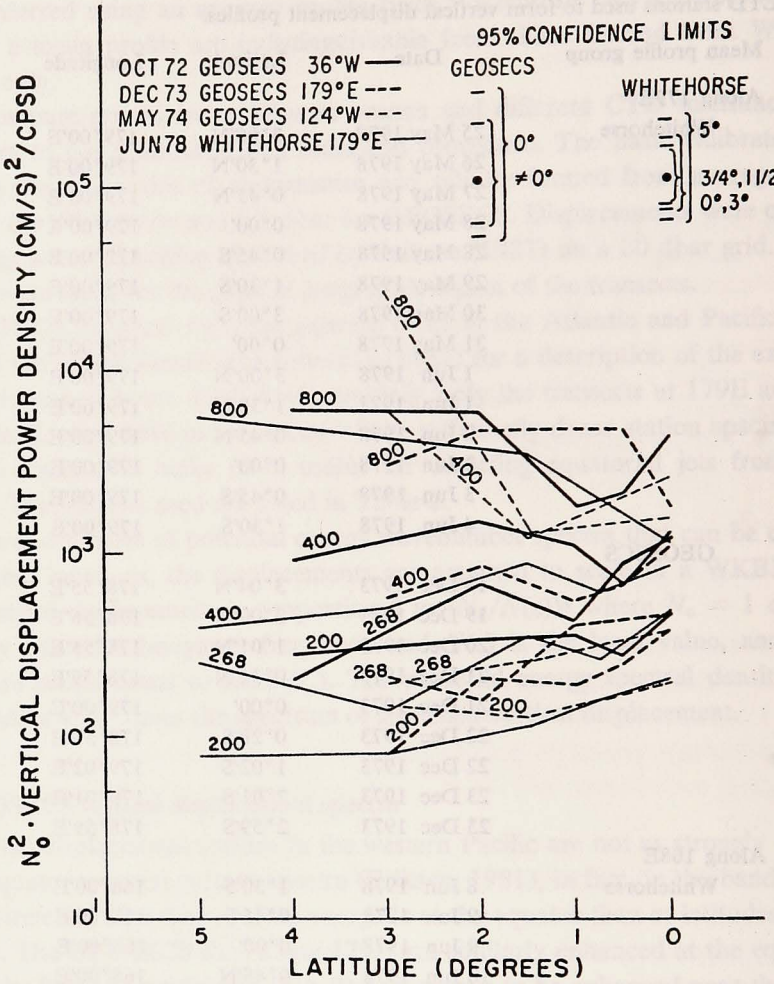

Figure 3. Autospectral estimates of twice the potential energy density per unit mass as a function of latitude. Numbers denote wavelengths in stretched dbar. Error bars are computed as in Figure 2.

We cannot say which of the regions (eastern or western Pacific or western Atlantic) is most energetic in vertical displacement because of wide confidence intervals. The estimates differ within two degrees of the equator by about a factor of five or less in energy. Similar energy levels are found by Hayes (1981) along 110W in the eastern Pacific. Thus we cannot claim to observe geographical changes in deep jet amplitudes.

As mentioned earlier, maximum displacement energy at the equator implies geostrophic currents which lag vertical displacement by $\pi/2$ with depth, which is what

occurs for the GEOSECS data. This is a characteristic of a wave disturbance with an eastward energy flux (e.g., Kelvin wave). As the deformation radii listed in Table 1 imply, a station spacing of 3/4° in latitude barely samples the decay of a Kelvin wave from the equator adequately at the vertical scales of the deep jets.

7. Discussion

The geostrophic nature of the deep jets and enhancement of vertical displacement within a fraction of a degree of the equator is further evidence that their physics is basically that of equatorial Kelvin waves. Vertical displacement and dynamic height amount to two different characterizations of the potential energy signal of the deep jets. Since Kelvin waves are constrained to travel along slopes ω/N, low frequency waves cannot reach the deep ocean without reflection off basin walls or other topography if they are generated at the surface. Recent Whitehorse profiling results indicate deep jets qualitatively similar to those in the western Pacific exist all the way to the ocean bottom in the central Pacific (J. Luyten, personal communication). Models of the pathways through which energy reaches the very deep ocean in the form of short vertical scale Kelvin waves at long period have not been developed. Interaction with topography seems a likely mechanism, since the available free waves of large scale and low frequency are of two forms: Kelvin and nondispersive Rossby. These two classes carry energy in opposite directions along the equator; they are the natural products of topographic scattering. The pattern of deep equatorial current intensification is too broad at each wavenumber to be due solely to Kelvin waves, thus the interpretation by Eriksen (1981) that broader scale currents take the form of Rossby waves.

The general character of density profile information near the equator is about the same at the GEOSECS sites discussed as in the Whitehorse data. No deep current profiles have been made to date in the equatorial Atlantic. However, the results in Figure 3 suggest that deep jets exist there and were measured in 1972 the same way currents are extra-equatorially: via geostrophy. Equatorially confined deep jets appear to be a general feature of all equatorial oceans.

Acknowledgments. I thank R. T. Williams and his co-workers at the Physical and Chemical Oceanographic Data Facility of the Scripps Institution of Oceanography for preparing and furnishing the GEOSECS CTD data. I am indebted to Susan Johnson for making the many calculations and plots which form this study. I thank Kit O'Neill for carefully reviewing a draft of this manuscript and offering helpful suggestions. Thanks to P. Farrell for preparing the manuscript. This work was supported by the National Science Foundation Grant OCE-8024911. H. Bryden encouraged this study.

APPENDIX A

Zonal energy flux and coherence phases

The sign of the coherence phase of zonal current and vertical displacement with depth for equatorial waves depends on the product $U_n \cdot P_n$, as discussed in Section 2 of the text. The sign

of the product $U_n \cdot P_n$ determines whether vertical displacement leads ($U_n \cdot P_n > 0$) or lags ($U_n \cdot P_n < 0$) eastward current by $\pi/2$ with increasing depth. The product $U_n \cdot P_n$ is, in turn, related to zonal wavenumber.

Expressions for U_n and P_n, $n \geqslant 1$, in the notation of Eriksen (1980) are:

$$U_n(\eta) = A_n \left[- \frac{\left(\frac{n}{2}\right)^{\frac{1}{2}} \psi_{n-1}(\eta)}{\sigma + s} - \frac{\left(\frac{n+1}{2}\right)^{\frac{1}{2}} \psi_{n+1}(\eta)}{\sigma - s} \right] \tag{A1a}$$

$$P_n(\eta) = A_n \left[\frac{\left(\frac{n}{2}\right)^{\frac{1}{2}} \psi_{n-1}(\eta)}{\sigma + s} - \frac{\left(\frac{n+1}{2}\right)^{\frac{1}{2}} \psi_{n+1}(\eta)}{\sigma - s} \right] \tag{A1b}$$

where η, σ, and s are nondimensional latitude, frequency, and zonal wavenumber, respectively. The ψ_n are Hermite functions

$$\psi_n(\eta) = \frac{e^{-\eta^2/2} H_n(\eta)}{(2^n n!\, \pi^{\frac{1}{2}})^{\frac{1}{2}}} \tag{A2}$$

where $H_n(\eta)$ are the Hermite polynomials. Through the recurrence relation $\eta H_n = nH_{n-1} + \frac{1}{2}H_{n+1}$, an expression for the product of interest evaluated at the equator $\eta = 0$ is:

$$U_n(0) \cdot P_n(0) = 2\psi_{n-1}^2(0) A_n^2 \frac{n \sigma s}{(\sigma^2 - s^2)^2} \tag{A3}$$

The zonal wavenumber s is the only quantity in this expression which changes sign; whether eastward current lags or leads vertical displacement near the equator for Rossby and gravity modes depends solely on the direction of zonal phase propagation.

For the mixed Rossby-gravity ($n = 0$) and Kelvin ($n = -1$) modes, $U_n \equiv P_n$ so the product is positive. For even n, $U_n(0) = 0$; however, the product is an even function of latitude for all n, so the sign of $U_n \cdot P_n$ will remain the same from the equator out to the first zero crossing in either U_n or P_n. In practice, this means that the phase relation between u and ζ will remain fixed for a finite band of latitudes centered on the equator.

APPENDIX B

Kinetic and potential energy of equatorial Rossby waves

Evaluating the expressions (A1) in the previous Appendix in the limit of long (nondispersive) equatorial Rossby waves shows the tendency for potential energy to be much less than kinetic energy near the equator. In this limit, the nondimensional dispersion relation $\sigma^2 - s^2 - s/\sigma = 2n + 1$ becomes $s \approx -\sigma(2n + 1)$ so the expressions for zonal current U_n and pressure P_n become:

$$U_n \approx \frac{A_n}{\sigma} \left(\left(\frac{2}{n}\right)^{\frac{1}{2}} \psi_{n-1} - \left(\frac{2}{n+1}\right)^{\frac{1}{2}} \psi_{n+1} \right) \tag{B1a}$$

$$P_n \approx \frac{A_n}{\sigma} \left(- \left(\frac{2}{n}\right)^{\frac{1}{2}} \psi_{n-1} - \left(\frac{2}{n+1}\right)^{\frac{1}{2}} \psi_{n+1} \right) \tag{B1b}$$

The functions ψ_n are such that equatorward of the first nonequatorial zero crossing of ψ_{n-1}, $\psi_{n+1} \cdot \psi_{n-1} < 0$ at latitudes $y \neq 0$. The Hermite functions $V_n = A_n \psi_n$ graphed in Figure 14 of Eriksen (1981) show this property. Thus the magnitude U_n tends to be much greater than P_n near the equator as can be seen by inspection of (B1).

In the opposite limit, that of short waves, $s \approx -\frac{1}{\sigma}$, so (A1) become:

$$U_n \approx A_n \left(\sqrt{\frac{n}{2}}\ \psi_{n-1} - \sqrt{\frac{n+1}{2}}\ \psi_{n+1} \right) \tag{B2a}$$

$$P_n \approx A_n \sigma \left(-\sqrt{\frac{n}{2}}\ \psi_{n-1} - \sqrt{\frac{n+1}{2}}\ \psi_{n+1} \right) \tag{B2b}$$

These expressions have the same symmetry as (B1), so that likewise for short waves, P_n tends to be much smaller than U_n near the equator.

Long (short) Rossby wave currents are primarily zonal (meridional) near the equator and are considerably more energetic than the vertical displacement field (kinetic energy $\alpha\ U_n^2 + V_n^2$, potential energy $\alpha\ P_n^2$) near the equator in the limit of low frequency ($\sigma << (n + \frac{1}{2} - (n(n+1))^{\frac{1}{2}})^{\frac{1}{2}}$).

REFERENCES

Broecker, W. S. 1981. Geochemical tracers and ocean circulation, *in* Evolution of Physical Oceanography, B. A. Warren and C. Wunsch, eds., M.I.T. Press, Cambridge, MA, 434–460.

Eriksen, C. C. 1980. Evidence for a continuous spectrum of equatorial waves in the Indian Ocean. J. Geophys. Res., *85*, 3285–3303.

—— 1981. Deep currents and their interpretation as equatorial waves in the western Pacific Ocean. J. Phys. Oceanogr., *11*, 48–70.

Fofonoff, N. P., S. P. Hayes and R. C. Millard, Jr. 1974. WHOI/Brown CTD microprofiler: Methods of calibration and data handling. Woods Hole Oceanographic Institution, Tech. Rep. WHOI-74-89, Woods Hole, MA, 64 pp.

Hayes, S. P. 1981. Vertical finestructure observations in the eastern equatorial Pacific. J. Geophys. Res., *86*, 10983–10999.

Hayes, S. P. and H. B. Milburn. 1980. On the vertical structure of velocity in the eastern equatorial Pacific. J. Phys. Oceanogr., *10*, 633–635.

Koopmans, L. H. 1974. The Spectral Analysis of Time Series. Academic Press, 366 pp.

Luyten, J. R., G. Needell and J. Thomson. 1982. An acoustic dropsonde-design, performance and evaluation. Deep-Sea Res., *29*, 499–524.

Luyten, J. R. and J. C. Swallow. 1976. Equatorial undercurrents. Deep-Sea Res., *23*, 999–1001.

Moore, D. W. and S. G. H. Philander. 1977. Modeling of the tropical oceanic circulation, *in* The Sea: Ideas and Observations on Progress in the Study of the Seas, Vol. 6, Marine Modeling, E. D. Goldberg, I. N. McCave, J. J. O'Brien and J. H. Steele, eds., John Wiley, Interscience, 319–361.

Wunsch, C. and A. E. Gill. 1976. Observations of equatorially trapped waves in Pacific sea level variations. Deep-Sea Res., *23*, 371–390.

Received: *14 August, 1981*; revised: *22 January, 1982.*